

# A radiation-hydrodynamics scheme valid from the transport to the diffusion limit.

E. Audit\*, P. Charrier†, J.-P. Chièze\* and B. Dubroca‡

\* CEA/DSM/DAPNIA Service d'Astrophysique, CEA/Saclay 91191  
Gif-sur-Yvette Cedex, France

† Applied Mathematics, UMR-CNRS 5466, LRC-CEA M03, Université Bordeaux  
I, 33405 Talence

‡ CEA-CESTA, BP2, 33114 Le Barp

E-mail: Edouard.Audit@cea.fr, Pierre.Charrier@math.u-bordeaux.fr,  
jpchieze@cea.fr, Bruno.Dubroca@cea.fr

Version: May 7, 2002

We present in this paper the numerical treatment of the coupling between hydrodynamics and radiative transfer. The fluid is modeled by classical conservation laws (mass, momentum and energy) and the radiation by the grey moment  $M_1$  system [5]. The scheme introduced is able to compute accurate numerical solution over a broad class of regimes from the transport to the diffusive limits. We propose an asymptotic preserving modification of the HLLE scheme in order to treat correctly the diffusion limit. Several numerical results are presented, which show that this approach is robust and have the correct behavior in both the diffusive and free-streaming limits. In the last numerical example we test this approach on a complex physical case by considering the collapse of a gas cloud leading to a proto-stellar structure which, among other features, exhibits very steep opacity gradients.

*Key Words:* Radiative transfer; radiation-hydrodynamics; diffusion limit; transport; hyperbolic system; Godunov-type methods

## 1. INTRODUCTION

Radiation hydrodynamics plays an important role in astrophysics, laser fusion and plasma physics. For many years, efforts have been underway to develop mathematical models and numerical schemes to obtain accurate predictions at reasonable computing cost in this domain.

One of the main difficulty is to obtain accurate numerical computations in the various regimes that can be encountered due to values of material opacities which can vary from several order of magnitude. This can be achieved by using the full radiative transfer equation but it is still out of range for complex simulations in particular in two or three spatial dimensions. To overcome this difficulty several models have been derived. For large values of the material opacity, an asymptotic analysis leads to hyperbolic/parabolic systems of equation refered to as the equilibrium-diffusion limit or non equilibrium diffusion approximation ([12],[11], [10], [2]). On the other hand, for smaller values of the opacity the streaming limit can be handled by using an hyperbolic system of equations coupling some closure of the moment system of the transfer equation with the hydrodynamic system ([12],

[11], [10],[1]) . Unfortunately for several real applications, such as radiative shocks or star formation, very different regimes are encountered in the same simulation. Coupling different models on various zones introduces large drawbacks due to the domain partition and some loss of accuracy in the transitional zone.

From a numerical point of view high-resolution schemes are necessary to take into account the different space and time scales. Godunov-type schemes based on exact or approximate Riemann solvers are efficient for shock problems ([7], [14], [13]). In radiation hydrodynamics, without source terms, hydrodynamic and radiation equations decouple so that a Riemann solver for the entire system can easily be derived from Riemann solvers for the hydrodynamic subsystem and for the radiation subsystem. Nevertheless, the difficulty of this approach is to obtain the correct diffusion limit for the scheme and correct behavior in transitional regime. Let us notice that the regime at the numerical level depends on the ratio of the mean free path of photons and the size of the local cell. An other difficulty is related to the time scales in the considered problems. In most cases radiation has to be treated implicitly since the time step given by usual CFL condition is much too small. When possible the hydrodynamics may be treated explicitly ([3]), but in some problems the time step given by the CFL condition on the hydrodynamic subsystem is still too restrictive and hence a fully implicit approach is necessary.

In this paper we propose new model and numerical scheme to describe radiation hydrodynamics in a wide range of regimes. The equations for the fluid are the classical conservation laws (mass, momentum and energy). The radiation is described by the grey moment system of the transfer equation (radiative energy and radiative flux) with the  $M_1$  closure introduced in ([5]). This closure, based on the minimum entropy principle, is able to describe large anisotropy of the radiation while giving also the correct diffusion limit. The Eddington factor is a non constant function of the reduce flux and therefore the radiation subsystem is a nonlinear hyperbolic system. Here, these equations are written in the comoving frame, introducing some non conservative coupling terms. A Riemann solver is developped by performing a wave decomposition neglecting the nonconservative coupling terms and the source terms, which is trivial since the two subsystems then decouple. Afterwards the nonconservative terms are reintroduced in the scheme, by using in the radiation equations the velocity given by the hydrodynamic solver. This approach, natural in the streaming regime, can be improved to capture the diffusion limit. For that purpose the Riemann solver for the  $M_1$  subsystem is modified to take into account the stiff relaxation term along the ideas developped in ([8]). With this modification our approach is able to correctly treat the streaming regime as well as the diffusion regime with the same solver. Finally as radiative shocks or star formation simulations need high resolution and very different time scales we describe the implementation of our radiation hydrodynamics solver in a moving grid-time implicit framework.

The outline of this paper is as follows. In the second section the equations of radiation hydrodynamics with the  $M_1$ -closure are given. In section 3 we present the numerical methods for solving these equations. The actual implementation is detailed in section 4. Numerical experiments are shown in section 5, first on radiative shocks to demonstrate the validity of our method in various regime, then on the collapse of a gas cloud leading to a stellar-like structure. The last section is the conclusion of the paper.

## 2. THE PHYSICAL MODEL

The equations of grey radiative hydrodynamics under the assumption of local thermodynamic equilibrium can be found in ([11]). We have choosen in this work to use the radiative equation in the fluid (or comoving) frame :

$$\partial_t \rho + \nabla \cdot [\rho u] = 0 \quad (1)$$

$$\partial_t \rho u + \nabla \cdot [\rho u \otimes u + P \mathbf{I}] = \frac{\kappa}{c} \rho F_r + F \quad (2)$$

$$\partial_t E + \nabla \cdot [u(E + P)] = -\kappa \rho c (a_r T^4 - E_r) + (\frac{\kappa}{c} \rho F_r + F) \cdot u \quad (3)$$

$$\partial_t E_r + \nabla \cdot [E_r u] + \nabla \cdot F_r + \mathbf{P}_r : \nabla u = \kappa \rho c (a_r T^4 - E_r) \quad (4)$$

$$\partial_t F_r + \nabla \cdot [F_r u] + c^2 \nabla \cdot \mathbf{P}_r + (F_r \cdot \nabla) u = -\kappa \rho c F_r \quad (5)$$

where  $\rho$  is the matter density,  $u$  the velocity,  $E$  the total matter energy density,  $P$  and  $T$  the pressure and the temperature of the material,  $F$  the force density,  $E_r$  the radiative energy density,  $F_r$  the radiative flux,  $\mathbf{P}_r$  the radiative pressure tensor and  $\kappa$  the mean opacity.

The first part of the system (1)-(3) describe the evolution of the matter and the second one (4)-(5) the evolution of the radiation. These two fluids are coupled by the exchange of energy and momentum through respectively the  $\kappa \rho c (a_r T^4 - E_r)$  and  $\kappa \rho F_r / c$  terms.

In order to close system (1)-(5) it is necessary to give two equations of state for the flow and for the radiation. For the flow fields we assume a  $\gamma$ -law  $p = (\gamma - 1) \rho \varepsilon$  (with  $\gamma = 5/3$  in our applications). For the radiation fields we need a closure relation giving the radiative pressure  $\mathbf{P}_r$  in term of the radiative energy  $E_r$  and of the radiative flux  $F_r$ . A rather simple closure is to assume that the radiative flux is isotropic which leads to the closure  $\mathbf{P}_r = \frac{1}{3} E_r \mathbf{I}$ . Such an approximation is by construction not very well suited to model flow containing large anisotropy in the radiative flux which is generally the case for radiative shocks. We will therefore use the closure given by the  $M1$  model [5]. In this model, the radiative pressure is given by:

$$\mathbf{P}_r = \mathbf{D} E_r \quad (6)$$

where the Eddington tensor  $\mathbf{D}$  is defined by:

$$\mathbf{D} = \frac{1 - \chi}{2} \mathbf{I} + \frac{3\chi - 1}{2} n \otimes n \quad (7)$$

$$\chi = \frac{3 + 4|f|^2}{5 + 2\sqrt{4 - 3|f|^2}} \quad (8)$$

$\mathbf{I}$  is the identity matrix,  $\chi$  the Eddington factor,  $f = \frac{F_r}{c E_r}$  the reduced flux and  $n = f/|f|$  is a unit vector aligned with the radiative flux.

Let us remark that we can write the conservation of total (i.e. radiative and material) momentum and energy. Neglecting terms in  $(u/c)^2$  and terms involving the fluid acceleration this leads to the following equations

$$\partial_t(\rho u + \frac{1}{c^2} F_r) + \nabla \cdot [\rho u \otimes u + P \mathbf{I} + \mathbf{P}_r + u \frac{F_r}{c^2}] = F - (\frac{F_r}{c^2} \cdot \nabla) u \quad (9)$$

$$\partial_t(E + E_r + u \frac{F_r}{c^2}) + \nabla \cdot [u(E + E_r + P + P_r) + F_r] = F \cdot u \quad (10)$$

Some authors make the choice to discretize directly the total mass, momentum and energy conservation equations with either the material or radiative momentum and energy equations to close the system. In this paper we prefer to work with the system (1)-(5) where the flow and the radiation play a more symmetric role. The coupling between the flow and the radiation is done by the relaxation source terms and by the terms introduced by the comoving frame. The mathematical analysis of the hyperbolicity of this system do not take into account the source terms. The Jacobian  $\mathcal{A}$  of the system (1)-(5) can be written

$$\mathcal{A} = \begin{pmatrix} \mathcal{A}_{hh} & \mathcal{A}_{hr} \\ \mathcal{A}_{rh} & \mathcal{A}_{rr} \end{pmatrix} \quad (11)$$

where the blocks are associated with the partitioning of unknowns between hydrodynamic variables (denoted  $h$ ) and radiative variables (denoted  $r$ ). The hydrodynamic diagonal block  $\mathcal{A}_{hh}$  is classical and writes

$$\mathcal{A}_{hh} = \begin{pmatrix} 0 & 1 & 0 \\ (\gamma - 3) \frac{u^2}{2} & -(\gamma - 3)u & \gamma - 1 \\ -u \left( H - (\gamma - 1) \frac{u^2}{2} \right) & H - (\gamma - 1)u^2 & u\gamma \end{pmatrix} \quad (12)$$

where  $H = \epsilon + p/\rho + u^2/2$  is the total enthalpy of the flow. Since the radiative variables do not appear in the left-hand-side of the hydrodynamic equations we have

$$\mathcal{A}_{hr} = \begin{pmatrix} 0 & 0 \\ 0 & 0 \\ 0 & 0 \end{pmatrix}, \quad (13)$$

The radiative diagonal block  $\mathcal{A}_{rr}$  for the M1 subsystem in the comoving frame depends on the velocity of the flow and writes

$$\mathcal{A}_{rr} = \begin{pmatrix} u & 1 \\ c^2(\chi(f) - \chi'(f)f) & u + c\chi'(f) \end{pmatrix}. \quad (14)$$

Finally, the off-diagonal block due to the influence of hydrodynamic on the left-hand side of the radiative equations can be stated

$$\mathcal{A}_{rh} = \frac{1}{\rho} \begin{pmatrix} -u(E_r + P_r) & (E_r + P_r) & 0 \\ -uF_r & F_r & 0 \end{pmatrix}. \quad (15)$$

Since the jacobian matrix  $\mathcal{A}$  is a block lower triangular matrix its spectrum can easily be computed and is composed of the eigenvalues of the hydrodynamic subsystem, i.e.  $u - a$ ,  $u$ ,  $u + a$ , where  $a$  is the speed of sound and of  $\lambda_- + u$  and  $\lambda_+ + u$  where  $\lambda_-$  and  $\lambda_+$  are the eigenvalues of the M1-radiation subsystem in the laboratory frame (cf. [5] and section 3.3). We remark that the nonconservative coupling terms ( $\mathbf{P}_r : \nabla u$  and  $F_r \cdot \nabla u$ ) appear only in the off-diagonal block  $\mathcal{A}_{rh}$  and thus do not influence the signal velocities of the whole system.

### 3. NUMERICAL TREATMENT

The nonconservative form of the radiation-hydrodynamics system prevents using classical Godunov type scheme without care. In this paper we focus on some applications such as radiative shocks or collapse of a gas cloud where various regime are encountered in the same simulations.

Our numerical strategy is the following. The conservative system obtained by dropping the nonconservative coupling terms is discretized by a Godunov-type scheme based on a Riemann solver and the nonconservative terms are discretized using the same values as in this Riemann solver *at the same time step*. As we will see in the next sections the construction of the Riemann solver for the conservative system is quite simplified by the lower triangular structure and merely reduces to the construction of two decoupled Riemann solvers for the hydrodynamic and radiation subsystems.

The relaxation terms introduce an other kind of difficulty. For large value of the opacity they are stiff and an asymptotic analysis shows that the total energy is governed by a diffusion equation. This regime is commonly referred to as the equilibrium-diffusion limit ([11],[12]). To capture this regime with the above system we must treat carefully the relaxation terms using an asymptotic preserving scheme following the ideas introduced in ([8]). This will be detailed in section 3.3.2. Finally equations (1), (9) and (10) show that in a stationnary shock between two states where radiation is in equilibrium with material, the two states satisfy Rankine-Hugoniot relations involving both the radiative and material quantities. We will show in sections 5.1 and 5.2 that our numerical scheme satisfies these relations even when there is large energy transfer between matter and radiation.

In many astrophysical situations physical quantities vary over many orders of magnitude in a very steep way. To deal with such situations, the adaptive grid technic proposed by Dorfy and Drury [4] (thereafter DD) is very well suited. We have therefore choosen to implement our radiative-hydrodynamical scheme on such a grid. However, the numerical schemes presented below can also be applied on a static eulerian grid which would be better suited for multi-dimensionnal simulations.

Let us first start with some general remarks and notations. Space is discretized into computational zones centered on points  $r_i$ . The grid interfaces are located at  $r_{i\pm\frac{1}{2}}$ . The volume of a zone is given by:

$$\Delta v_i = \begin{cases} \frac{4}{3}\pi(r_{i+\frac{1}{2}}^3 - r_{i-\frac{1}{2}}^3) & \text{in spherical geometry} \\ r_{i+\frac{1}{2}} - r_{i-\frac{1}{2}} = \Delta r_i & \text{in slab geometry (assuming a unit surface)} \end{cases}$$

Subscripts  $(i, i + \frac{1}{2}, i + 1\dots)$  always stand for the space coordinates, while superscripts  $(n, n + \frac{1}{2}\dots)$  indicate time. Variables at time  $n + \frac{1}{2}$  are defined by:

$$X_i^{n+\frac{1}{2}} = (1 - \alpha)X_i^n + \alpha X_i^{n+1} \quad \alpha \in [0, 1]$$

for  $\alpha = 0$  the scheme will be explicit and for  $\alpha = 1$  it will be fully implicit. We also introduce the following notations which are useful to have more compact equations:

$$X_{[i\pm\frac{1}{2}]} = (X_{i+\frac{1}{2}} - X_{i-\frac{1}{2}}) \quad \text{and} \quad X^{[n]} = (X^{n+1} - X^n)$$

Subscript and superscript are always *distributive*:

$$(XY)_{[i \pm \frac{1}{2}]}^n = X_{i+\frac{1}{2}}^n Y_{i+\frac{1}{2}}^n - X_{i-\frac{1}{2}}^n Y_{i-\frac{1}{2}}^n$$

### 3.1. The grid

In the following, we briefly summarize the adaptive grid method of DD. The grid concentration is defined by:

$$n_i = \frac{L}{r_{i+\frac{1}{2}} - r_{i-\frac{1}{2}}}$$

where  $L$  is a typical length. If  $L$  is a constant, a uniform concentration corresponds to a uniform grid and if  $L = r_i$  a uniform concentration corresponds to a logarithmic grid. This later case is useful for spherical geometry.

The basic idea of DD is to demand that  $n$  is proportional to a resolution function  $\mathcal{R}$ . This means that there will be a large number of gridpoints wherever the resolution function is large. The resolution function depends on the nature of the problems being solved, but it is most of the time a function of the magnitude of the gradient of the physical quantities in order to have a large number of gridpoints where there are steep features in the flow.

In order for the grid to be computationally tractable it is also necessary to ensure that adjacent zones have roughly the same size and that the grid adaptation time is not too small compared to physical time scale. These two conditions are fulfilled using the following equation:

$$\hat{n}_i = n_i - \alpha_g(\alpha_g + 1)(n_{i-1} - 2n_i + n_{i+1}) \quad (16)$$

$$\tilde{n}_i^n = \hat{n}_i^n + \frac{\tau_g}{\Delta t}(\hat{n}_i^n - \hat{n}_i^{n-1}) \quad (17)$$

where  $\alpha_g$  is the grid rigidity and  $\tau_g$  the grid time-scale. Equation (16) ensures that the grid concentration does not vary from more than a factor  $(\alpha_g + 1)/\alpha_g$  between to adjacent zones and equation (17) set the time-scale on which the grid can readjust itself.

The final form of the grid equation is then:

$$\frac{\tilde{n}_{i+1}}{\mathcal{R}_{i+1}} = \frac{\tilde{n}_i}{\mathcal{R}_i} \quad (18)$$

This equation depends both on the grid coordinates  $r_i$  and on the physical quantities entering the resolution function  $\mathcal{R}$ .

### 3.2. The hydrodynamics

In one dimension and taking into account the moving grid equations (1)-(3) can be written:

$$\left\{ \begin{array}{lcl} \partial_t \rho S + \partial_r [\rho S(u - u_g)] & = & 0 \\ \partial_t \rho S u + \partial_r [\rho S u(u - u_g) + P S] & = & P \partial_r S + S(\frac{\kappa}{c} \rho F_r + F) \\ \partial_t E S + \partial_r [E S(u - u_g) + P S u] & = & -S \kappa \rho c (a_r T^4 - E_r) \\ & & -S(\frac{\kappa}{c} \rho F_r + F).u \end{array} \right. \quad (19)$$

where  $u_g$  is the grid velocity and the surface  $S$  equals 1 in slab geometry and  $4\pi r^2$  in spherical geometry.

The left hand side of system (19) is an hyperbolic system for the variables  $\rho S$ ,  $\rho S u$  and  $SE$ . Now, by introducing the moment vector  $\mathcal{U} = (\rho, \rho u, E)$  and the physical flux vector  $\mathcal{F}(\mathcal{U}) = (\rho u, p + \rho u^2, u(E + P))$ , the hyperbolic part of system (19) can be written under the following form:

$$\partial_t (S\mathcal{U}) + \partial_r [S(\mathcal{F}(\mathcal{U}) - u_g S\mathcal{U})] = 0. \quad (20)$$

As the physical flux vector is a degree one homogeneous vector valued function ( $S\mathcal{F}(\mathcal{U}) = \mathcal{F}(S\mathcal{U})$ ), if we set  $\hat{\mathcal{U}} = S\mathcal{U}$ , the hyperbolic part (20) can be rewritten as:

$$\partial_t \hat{\mathcal{U}} + \partial_r (\mathcal{F}(\hat{\mathcal{U}}) - u_g \hat{\mathcal{U}}) = 0. \quad (21)$$

The system (21) can be solved using an exact Riemann solver (Godunov scheme):

$$\frac{1}{\Delta t} (\hat{\mathcal{U}} \Delta r)_i^{[n]} + (\mathcal{F}(\hat{\mathcal{U}}^*) - u_g \hat{\mathcal{U}}^*)_{[i \pm \frac{1}{2}]}^{n+\frac{1}{2}} = 0 \quad (22)$$

The state  $\hat{\mathcal{U}}_{i+\frac{1}{2}}^*$  is the solution on the line  $r/t = 0$  of the Riemann problem between the cell  $i$  and  $i + 1$  involving the following initial conditions:

$$\begin{cases} \hat{\mathcal{U}}(0, r) = S_{i+\frac{1}{2}} U_{i+\frac{1}{2}}^- & \text{for } r < 0, \\ \hat{\mathcal{U}}(0, r) = S_{i+\frac{1}{2}} U_{i+\frac{1}{2}}^+ & \text{for } r > 0, \end{cases} \quad (23)$$

where  $S_{i+\frac{1}{2}}$  is the surface associated with interface  $i + \frac{1}{2}$ .  $U_{i+\frac{1}{2}}^-$  and  $U_{i+\frac{1}{2}}^+$  are the trace of  $U$  from the cell  $i$  and  $i + 1$ . For a first order scheme (no Van-Leer extrapolation)  $U_{i+\frac{1}{2}}^- = U_i$  and  $U_{i+\frac{1}{2}}^+ = U_{i+1}$ . (for details about the solution of the Riemann problem see [14])

We can note that we have used the solution of Riemann problem based on  $\mathcal{F}(\hat{\mathcal{U}}) - u_g \hat{\mathcal{U}}$  instead of  $\mathcal{F}(\hat{\mathcal{U}})$  flux. In fact, by the Galilean invariance of Euler equations, the solution of Riemann problem for  $\mathcal{F}(\hat{\mathcal{U}}) - u_g \hat{\mathcal{U}}$  flux on  $r/t = 0$  is the same as the solution of Riemann problem for  $\mathcal{F}(\hat{\mathcal{U}})$  flux on  $r/t = u_g$ .

Unfortunately, the uniform flow is not a numerical solution of the scheme (22). To satisfy this property, the mesh geometry must be solution of a balance equation called geometric conservation law (GCL):

$$\frac{1}{\Delta t} (S \Delta r)_i^{[n]} - (S u_g)_{[i \pm \frac{1}{2}]}^{n+\frac{1}{2}} = 0. \quad (24)$$

Of course, this relation is false for the spherical case. Moreover, if the product  $S_i \Delta r_i$  has been replaced by the volume of a cell  $\Delta v_i$ , a new numerical scheme is obtained which satisfies a GCL balance law:

$$\frac{1}{\Delta t} (\Delta v)_i^{[n]} - (S u_g)_{[i \pm \frac{1}{2}]}^{n+\frac{1}{2}} = 0, \quad (25)$$

$$\frac{1}{\Delta t} (\mathcal{U} \Delta v)_i^{[n]} + (\mathcal{F}(\hat{\mathcal{U}}^*) - u_g \hat{\mathcal{U}}^*)_{[i \pm \frac{1}{2}]}^{n+\frac{1}{2}} = 0. \quad (26)$$

The uniform flows are numerical solutions of the scheme (26). Hence, the whole numerical scheme about system (19) can be written now under the following form:

$$\frac{1}{\Delta t} \left( \rho \Delta v \right)_i^{[n]} + \left( \rho^* (u^* - u_g) \right)_{[i \pm \frac{1}{2}]}^{n+\frac{1}{2}} = 0 \quad (27)$$

$$\begin{aligned} \frac{1}{\Delta t} \left( \rho u \Delta v \right)_i^{[n]} + \left( \rho^* u^* (u^* - u_g) + P^* \right)_{[i \pm \frac{1}{2}]}^{n+\frac{1}{2}} = \\ \left( \partial_r S P \Delta r + \left( \frac{\kappa}{c} \rho F_r + F \right) \Delta v \right)_i^{n+\frac{1}{2}} \end{aligned} \quad (28)$$

$$\begin{aligned} \frac{1}{\Delta t} \left( E \Delta v \right)_i^{[n]} + \left( E^* (u^* - u_g) + P^* u^* \right)_{[i \pm \frac{1}{2}]}^{n+\frac{1}{2}} = \\ \left( (\kappa \rho c (a_r T^4 - E_r) + \left( \frac{\kappa}{c} \rho F_r + F \right) u) \Delta v \right)_i^{n+\frac{1}{2}} \end{aligned} \quad (29)$$

### 3.3. Solving for the radiative transfer

To simplify the presentation, we will first study the radiative transfer in a frozen medium and in a slab geometry. In this case, system (4)-(5) gives

$$\partial_t E_r + \partial_x F_r = \sigma c (a T_m^4 - E_r) \quad (30)$$

$$\partial_t F_r + c^2 \partial_x \mathbf{P}_r = -\sigma c F_r \quad (31)$$

where we have defined  $\sigma = \kappa \rho$ . Using the  $M_1$  closure, the radiative pressure is given by :

$$\mathbf{P}_r = \chi E_r = \frac{3 + 4f^2}{5 + 2\sqrt{4 - 3f^2}} E_r \quad \text{where} \quad f = \frac{F_r}{c E_r} \quad (32)$$

The previous system is a hyperbolic one which can be written under the following form:

$$\partial_t \mathcal{U} + \partial_x \mathcal{F}(\mathcal{U}) = \mathcal{S}(\mathcal{U}) \quad (33)$$

with

$$\mathcal{U} = \begin{pmatrix} E_r \\ F_r \end{pmatrix} \quad \mathcal{F}(\mathcal{U}) = \begin{pmatrix} F_r \\ c^2 \chi E_r \end{pmatrix} \quad \mathcal{S}(\mathcal{U}) = \begin{pmatrix} \sigma c (a T_m^4 - E_r) \\ -\sigma c F_r \end{pmatrix} \quad (34)$$

$\mathcal{U}$  is the moment vector,  $\mathcal{F}$  the physical flux vector and  $\mathcal{S}$  the source term vector. The Jacobian matrix  $J$  of this system is a function of  $f$  and  $c$  and is given by:

$$\mathbf{J}(\mathcal{U}) = \frac{\partial \mathcal{F}(\mathcal{U})}{\partial \mathcal{U}} = \begin{pmatrix} 0 & 1 \\ c^2 (\chi(f) - \chi'(f)f) & c \chi'(f) \end{pmatrix}$$

The eigenvalues,  $\lambda^-$ ,  $\lambda^+$  ( $\lambda^- < \lambda^+$ ) of the matrix  $\mathbf{J}$  can now be calculated:

$$\lambda^- = \frac{\chi'(f) - \sqrt{\chi'(f)^2 - 4f\chi'(f) + 4\chi(f)}}{2} c, \quad (35a)$$

$$\lambda^+ = \frac{\chi'(f) + \sqrt{\chi'(f)^2 - 4f\chi'(f) + 4\chi(f)}}{2} c. \quad (35b)$$

The eigenvalues,  $\lambda^-$  and  $\lambda^+$ , of  $\mathbf{J}$  are plotted in figure [1-A]. At radiative equilibrium (when  $f = 0$ ), the eigenvalues are equal to  $\pm c/\sqrt{3}$ , which is a direct consequence of the isotropy of underlying distribution function of the photons. On the other hand, in the case of extreme non-equilibrium, when  $f = 1$  (resp.  $f = -1$ ), the eigenvalues are degenerated and are equals to  $c$  (resp.  $-c$ ). This case corresponds to the free-streaming limit where all the photons move towards the same direction. It is important to note that in the case of a constant Eddington factor ( $\chi = 1/3$ ), the eigenvalues are also constant and equal to  $\pm c/\sqrt{3}$ , which means that a light front can not propagate at the speed of light, as it should.

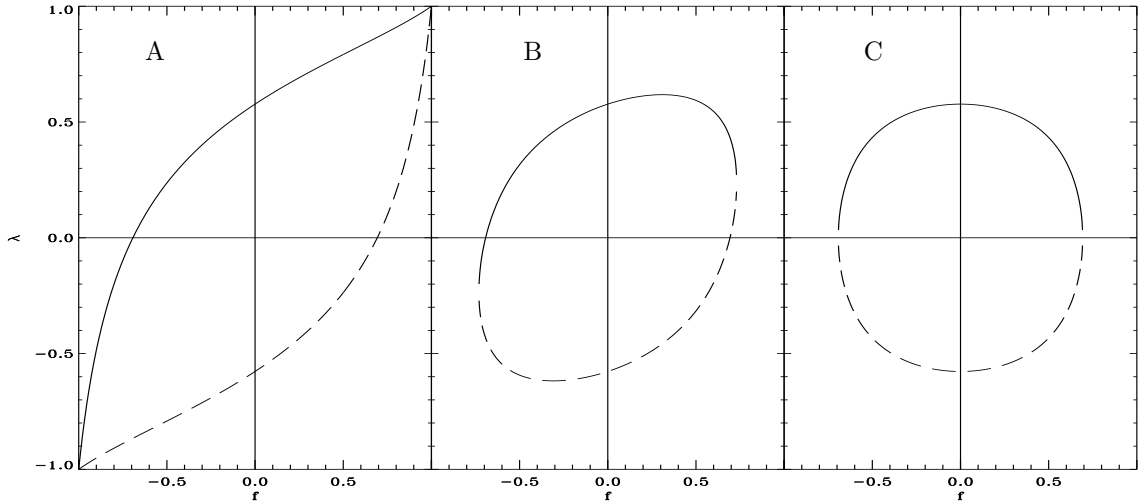


**FIG. 1** eigenvalues of  $M_1$ ,  $\frac{\lambda^+}{c}$  (full line) and  $\frac{\lambda^-}{c}$  (dashed line) according to  $f = \frac{F_r}{cE_r}$ , the normalized flux for  $\epsilon = 1$  (A),  $\epsilon = 0.5$  (B) and  $\epsilon = 0$  (C),

### 3.3.1. Numerical approximation of $P_1$ and $M_1$ by the HLLE approximate Riemann solver

The system (30)-(31) can be discretized using a Godunov method based on the HLLE approximate Riemann solver (see [6]). Hence, we need to find an estimation of the largest and smallest physical signal-velocities in the exact solution to the Riemann problem. This estimation involves the eigenvalues of the Roe's linearization for the  $M_1$  model. The  $M_1$  Roe's matrix  $\mathbf{J}_{i+\frac{1}{2}}$  between  $i$  and  $i + 1$  states can be written as:

$$\mathbf{J}_{i+\frac{1}{2}} = \begin{pmatrix} 0 & 1 \\ c^2(\chi_a - \chi'_m f_a) & c\chi'_m \end{pmatrix},$$

where

$$f_a = \frac{f_i + f_{i+1}}{2}, \quad \chi_a = \frac{\chi(f_i) + \chi(f_{i+1})}{2}, \quad \chi'_m = \begin{cases} \frac{\chi(f_{i+1}) - \chi(f_i)}{f_{i+1} - f_i} & \text{if } f_i \neq f_{i+1}, \\ \chi'(f_i) & \text{else.} \end{cases}$$

The eigenvalues,  $\lambda_{i+\frac{1}{2}}^-, \lambda_{i+\frac{1}{2}}^+ (\lambda_{i+\frac{1}{2}}^- < \lambda_{i+\frac{1}{2}}^+)$  of the matrix  $\mathbf{J}_{i+\frac{1}{2}}$  can now be calculated:

$$\lambda_{i+\frac{1}{2}}^- = \frac{\chi'_m - \sqrt{\chi'^2 - 4f_a\chi'_m + 4\chi_a}}{2} c, \quad (36a)$$

$$\lambda_{i+\frac{1}{2}}^+ = \frac{\chi'_m + \sqrt{\chi'^2 - 4f_a\chi'_m + 4\chi_a}}{2} c. \quad (36b)$$

Once knowing the numerical signal velocities  $\lambda_{i+\frac{1}{2}}^\pm$ , the numerical flux function  $\mathcal{F}_{i+\frac{1}{2}}$  between cells  $i$  and  $i+1$  can be written under the following form:

$$\mathcal{F}_{i+\frac{1}{2}} = \frac{a^+ \mathcal{F}_i - a^- \mathcal{F}_{i+1} + a^+ a^- (\mathcal{U}_{i+1} - \mathcal{U}_i)}{a^+ - a^-} \quad \text{where} \quad \begin{cases} a^+ = \max(\lambda_{i+1}^+, \lambda_{i+\frac{1}{2}}^+, 0), \\ a^- = \min(\lambda_i^-, \lambda_{i+\frac{1}{2}}^-, 0). \end{cases}$$

The system (30)-(31) can then be discretized in conservative form:

$$\frac{E_{r,i}^{n+1} - E_{r,i}^n}{\Delta t} + \frac{F_{r,i+\frac{1}{2}}^{n+\frac{1}{2}} - F_{r,i-\frac{1}{2}}^{n+\frac{1}{2}}}{\Delta x} = \sigma_i^{n+\frac{1}{2}} c (a_r T_m^4 - E_{r,i}^{n+\frac{1}{2}}) \quad (37)$$

$$\frac{F_{r,i}^{n+1} - F_{r,i}^n}{\Delta t} + c^2 \frac{P_{r,i+\frac{1}{2}}^{n+\frac{1}{2}} - P_{r,i-\frac{1}{2}}^{n+\frac{1}{2}}}{\Delta x} = -\sigma_i^{n+\frac{1}{2}} c F_{r,i}^{n+\frac{1}{2}} \quad (38)$$

### 3.3.2. Scheme modification to enforce asymptotic limit

As we mentionned before, one of the important difficulties of radiative transfer is to be able to deal with very different regimes. It is therefore important to ensure that our scheme has the correct limiting behavior both in the free-streaming and diffusive regimes.

In order to illustrate these points in a simple manner we will consider wave speeds equal to the speed of light (i.e.  $a^+ = -a^- = c$ ) and a constant Eddington factor  $\chi = 1/3$  (resp. 1) in the diffusive (resp. free-streaming) regime. The discretized equations then take the following form:

$$\frac{E_{r,i}^{n+1} - E_{r,i}^n}{\Delta t} + \frac{F_{r,i+1}^{n+\frac{1}{2}} - F_{r,i-1}^{n+\frac{1}{2}}}{2\Delta x} - \frac{c}{2\Delta x} (E_{r,i+1}^{n+\frac{1}{2}} - 2E_i^{n+\frac{1}{2}} + E_{r,i-1}^{n+\frac{1}{2}}) = \sigma_i^{n+\frac{1}{2}} c (a_r T_m^4 - E_{r,i}^{n+\frac{1}{2}})$$

$$\frac{F_{r,i}^{n+1} - F_{r,i}^n}{\Delta t} + c^2 \chi \frac{E_{r,i+1}^{n+\frac{1}{2}} - E_{r,i-1}^{n+\frac{1}{2}}}{2\Delta x} - \frac{c}{2\Delta x} (F_{r,i+1}^{n+\frac{1}{2}} - 2F_{r,i}^{n+\frac{1}{2}} + F_{r,i-1}^{n+\frac{1}{2}}) = -\sigma_i^{n+\frac{1}{2}} c F_{r,i}^{n+\frac{1}{2}}$$

the modified equations actually solved by the numerical scheme are therefore:

$$\partial_t E_r + \partial_x F_r - \frac{c}{2} \Delta x \partial_x^2 E_r = \sigma c (a_r T_m^4 - E_r) \quad (39)$$

$$\partial_t F_r + c^2 \chi \partial_x E_r - \frac{c \Delta x}{2} \partial_x^2 F_r = -\sigma c F_r \quad (40)$$

### Free-streaming regime

Let us first consider the case of light freely propagating in vacuum (i.e.  $\sigma = 0$ ) with all the photons going in the same direction (i.e.  $F = cE$ ). The resulting equation for the energy of the radiation is then:

$$\partial_t E + c \partial_x E_r - \frac{c \Delta x}{2} \partial_x^2 E_r = 0. \quad (41)$$

This equation is the exact advection equation with an added numerical diffusion term. The single mode solutions of the exact equation are of the form:  $E_r = E_{r,0} \cos(2\pi/\lambda(ct - x))$ . For this mode and under CFL condition the variation of energy due to the diffusion term can be estimated:

$$\frac{\Delta E_r}{\Delta t} = \frac{4\pi^2}{2} E_{r,0} \frac{c \Delta x}{\lambda^2} \Rightarrow \frac{\Delta E_r}{E_{r,0}} = \frac{4\pi^2}{2} \frac{c \Delta t \Delta x}{\lambda^2} \sim \left(\frac{\Delta x}{\lambda}\right)^2$$

If the wave-length of the perturbation is properly sampled by the grid the diffusion term will always remain negligible. As could be expected, there will be some diffusion for very sharp energy profiles. In actual simulations, this diffusion will be further reduced by taking into account the proper waves speed and we will show in the next section that it remains acceptable.

### Diffusive regime

Let us now examine the diffusive regime. In this case, the temporal variation of the radiative flux can be neglected. Equation (40) then gives at first order:

$$F_r \simeq -\frac{c}{3\sigma} \partial_x E_r \quad (42)$$

inserting the previous expression into equation (39) one gets:

$$\partial_t E_r - \frac{c}{3\sigma} \left(1 + \frac{3\sigma \Delta x}{2}\right) \partial_x^2 E_r = \sigma c (a T_m^4 - E_r) \quad (43)$$

The equation obtained for  $E_r$  is indeed a diffusion equation. Furthermore, if the grid is sufficiently fine so that  $\sigma \Delta x \ll 1$ , the diffusion coefficient is the right one. On the other hand, if the grid does not sample the photon mean free path ( $\sigma \Delta x \gg 1$ ), the diffusion coefficient is then dominated by a purely numerical term and it is therefore much larger than it should. With this simple analysis it is possible to explain some of our numerical results. For a coarse grid, the effective diffusion coefficient is too large and the thermal precursor is therefore longer. This wrong behavior in the diffusive regime is not a characteristic of the HLLE scheme we have used. In any Godounov type method the divergence is discretized as the sum of a centered term and numerical diffusion term. This last term is absolutely necessary to ensure the stability of the scheme. Generally this term is proportional to  $\Delta x^n$ , ( $n = 1, 2$ ). When the mean free path of photon is much smaller than  $\Delta x$ , the numerical diffusion term can become dominant, as we have just seen.

In order to have a scheme which reproduces correctly the diffusion limit, it is therefore necessary to explicitly take into account the smallness of the photon mean free path. We present below such a scheme.

We first write the system of equation (30)-(31) in a dimensionless way. For that purpose we consider a characteristic length  $l$  and we defined the following quantities:

$$\epsilon = \frac{1}{\sigma l} \quad \tilde{t} = \frac{ct}{\sigma l^2} \quad \tilde{x} = \frac{x}{l} \quad \tilde{F}_r = \frac{F_r}{c\epsilon}$$

the system (30-31) can then be written:

$$\partial_{\tilde{t}} E_r + \partial_{\tilde{x}} \tilde{F}_r = \frac{(aT_m^4 - E_r)}{\epsilon^2} \quad (44)$$

$$\partial_{\tilde{t}} \tilde{F}_r + \frac{1}{\epsilon^2} \partial_{\tilde{x}} \chi E_r = -\frac{1}{\epsilon^2} \tilde{F}_r \quad (45)$$

The difficulty raised by the diffusive limit is highlighted in equation (45). When  $\epsilon$  is very small, the hyperbolic system (44)-(45) becomes very stiff because of the second term of equation (45) (the jacobian condition number  $\rightarrow \infty$  when  $\epsilon \rightarrow 0$ ). An interesting way to overcome this difficulty is to transform the previous system in a non-stiff hyperbolic system with stiff source term [8]. Equation (45) can be written :

$$\partial_{\tilde{t}} \tilde{F}_r + \partial_{\tilde{x}} \chi E_r = -\frac{1}{\epsilon^2} (\tilde{F}_r + (1 - \epsilon^2) \partial_{\tilde{x}} \chi E_r) \quad (46)$$

The new system to be integrated is now composed of equations (44) and (46). In order to integrate this system the hyperbolic terms (to the left of the equal sign) will be treated by the Godounov type method presented above, whereas the other terms (to the right of the equal sign) will be treated as source terms. Which means that they will be discretized in a purely centered manner. When  $\epsilon = 1$  the system (44)-(46) is identical to system (30)-(31) and gives the correct transport regime. But when  $\epsilon \rightarrow 0$ , the source term in equation (46) becomes dominant and gives the correct radiative flux in the diffusion limit. Furthermore, because of the change of  $F$  into  $\tilde{F}_r$ , the numerical diffusion term in equation (30) has been multiplied by  $\epsilon$  and will therefore always remain small.

The hyperbolic system to be solved is now:

$$\begin{cases} \partial_{\tilde{t}} E_r + \partial_{\tilde{x}} \tilde{F}_r = 0 \\ \partial_{\tilde{t}} \tilde{F}_r + \partial_{\tilde{x}} \chi E_r = 0 \end{cases} \quad (47)$$

As previously done, we will integrate the above system using a approximate HLLE Riemann solver. The Jacobian of the system (47) is:

$$\mathbf{J} = \begin{bmatrix} 0 & 1 \\ \chi - f\chi' & \epsilon\chi' \end{bmatrix} \quad \text{with } f = F_r/cE_r, \quad \chi = \chi(f) \quad \text{and} \quad \chi' = \frac{d\chi(f)}{df}$$

The eigenvalues,  $\tilde{\lambda}^+$  and  $\tilde{\lambda}^-$  ( $\tilde{\lambda}^+ > \tilde{\lambda}^-$ ), of the Jacobian are given by:

$$\tilde{\lambda}^{\pm} = \frac{(\epsilon\chi' \pm \sqrt{(\epsilon\chi')^2 + 4(\chi - f\chi')})}{2}$$

It is worth noticing that in order to keep the previous eigenvalues real one must have  $(\epsilon\chi')^2 + 4(\chi - f\chi') \geq 0$ . Therefore, for a given value of  $f$  there is a minimum possible value ( $\epsilon_{min}$ ) for the  $\epsilon$  parameter.  $(f\chi' - \chi)$  is an increasing function of  $f$  which vanishes for  $f = f_0 = 2\sqrt{3}/5$ . Thus, if  $f < f_0$  there is not constraint on the value of  $\epsilon$  (i.e.  $\epsilon_{min} = 0$ ) but if  $f > f_0$  there is a strictly positive minimum value for  $\epsilon$ . The function  $\epsilon_{min}(f)$  is plotted on figure (2). These limitations on  $\epsilon$  even though they have a mathematical origin, are physically justified since they imply that when the radiative flux is high one can not tend toward the diffusion scheme. Furthermore, we can deduce from system (47) and from the fact that the  $M_1$  model has an intrinsic flux limitation that  $\tilde{f} = \tilde{F}_r/cE_r \leq 1$ . It is therefore important to always keep  $\epsilon > f$  in order to compute correctly the radiative flux.

In this case, we need also to find as in the previous subsection an estimation of the largest and smallest physical signal velocities in the exact solution to the Riemann problem. This estimation involves the eigenvalues of the Roe's linearization for modified  $M_1$  model (47). The Roe's matrix  $\mathbf{J}_{i+\frac{1}{2}}$  for this model can be written under the following form:

$$\mathbf{J}_{i+\frac{1}{2}} = \begin{pmatrix} 0 & 1 \\ (\chi_a - \chi'_m f_a) & \epsilon \chi'_m \end{pmatrix},$$

where we have used the same notation as in the previous section. The eigenvalues  $\tilde{\lambda}_{i+\frac{1}{2}}^\pm$  of this matrix are:

$$\tilde{\lambda}_{i+\frac{1}{2}}^\pm = \frac{(\epsilon \chi'_m \pm \sqrt{(\epsilon \chi'_m)^2 + 4(\chi_a - f_a \chi'_m)})}{2}.$$

As in the previous case, one can give an estimation of the largest and smallest physical signal velocities:

$$\tilde{a}^+ = \max(\tilde{\lambda}_{i+1}^+, \tilde{\lambda}_{i+\frac{1}{2}}^+, 0), \quad \tilde{a}^- = \min(\tilde{\lambda}_i^-, \tilde{\lambda}_{i+\frac{1}{2}}^-, 0). \quad (48)$$

Using the HLLE solver gives the following expressions for the flux:

$$\tilde{F}_{r,i+\frac{1}{2}} = \frac{\tilde{a}^+ \tilde{F}_{r,i} - \tilde{a}^- \tilde{F}_{r,i+1}}{\tilde{a}^+ - \tilde{a}^-} + \frac{\tilde{a}^+ \tilde{a}^-}{\tilde{a}^+ - \tilde{a}^-} (E_{r,i+1} - E_{r,i}) \quad (49)$$

$$\tilde{P}_{r,i+\frac{1}{2}} = \frac{\tilde{a}^+ \tilde{P}_{r,i} - \tilde{a}^- \tilde{P}_{r,i+1}}{\tilde{a}^+ - \tilde{a}^-} + \frac{\tilde{a}^+ \tilde{a}^-}{\tilde{a}^+ - \tilde{a}^-} (\tilde{F}_{r,i+1} - \tilde{F}_{r,i}) \quad (50)$$

Rewriting the system in the original variables, we get the following discretisation for the  $M_1$  model:

$$\frac{1}{\Delta t} (E_r^{n+1} - E_r^n)_i + \frac{1}{\Delta r} (F_{r,i+\frac{1}{2}} - F_{r,i-\frac{1}{2}})^{n+\frac{1}{2}} = \sigma c (a_r T^4 - E_r)_i^{n+\frac{1}{2}} \quad (51)$$

$$\frac{1}{\Delta t} (F_r^{n+1} - F_r^n)_i + \frac{c^2}{\Delta r} (\hat{P}_{r,i+\frac{1}{2}} - \hat{P}_{r,i-\frac{1}{2}})^{n+\frac{1}{2}} = -\sigma c F_{r,i}^{n+\frac{1}{2}} \quad (52)$$

where we have defined:

$$\hat{P}_{r,i+\frac{1}{2}} = \epsilon^2 P_{r,i+\frac{1}{2}} + (1 - \epsilon^2)(P_{r,i+1} + P_{r,i})/2 \quad \text{and} \quad F_{r,i\pm\frac{1}{2}} = c\epsilon \tilde{F}_{r,i\pm\frac{1}{2}}$$

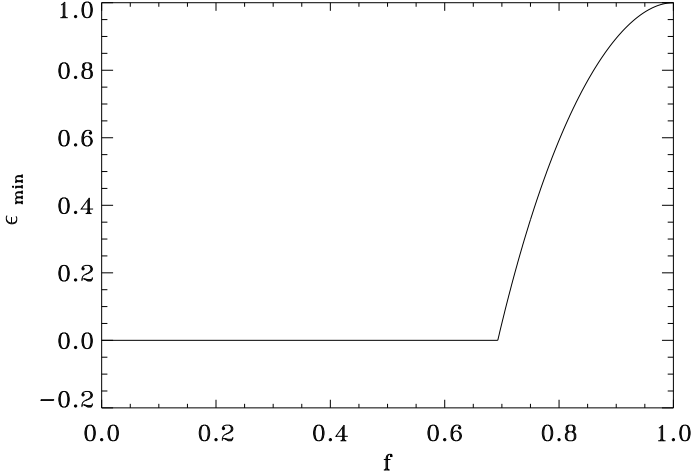


**FIG. 2** Minimum value of the  $\epsilon$  parameter in order to keep real the eigenvalues  $\tilde{\lambda}^+$  and  $\tilde{\lambda}^-$  plotted as a function of the reduce flux  $f = F_r/cE_r$ .

The method is easily extended to the radiation subsystem written in the co-moving frame but where the nonconservative terms are dropped and with a moving grid. The system then writes

$$\partial_t E_r + \partial_x((u - u_g)E_r) + \partial_x F_r = \sigma c(a_r T_m^4 - E_r), \quad (53)$$

$$\partial_t F_r + \partial_x((u - u_g)F_r) + c^2 \partial_x \mathbf{P}_r = -\sigma c F_r, \quad (54)$$

The non-conservative terms are dropped for the present analysis but they must naturally be taken into account as will be detailed in the next section. The previous system can be written in a dimensionless way

$$\partial_{\tilde{t}} E_r + \partial_{\tilde{x}} \left( \frac{\tilde{u}}{\epsilon} E_r + \tilde{F}_r \right) = \frac{(a T_m^4 - E_r)}{\epsilon^2}, \quad (55)$$

$$\partial_{\tilde{t}} \tilde{F}_r + \frac{1}{\epsilon^2} \partial_{\tilde{x}} \chi E_r + \frac{1}{\epsilon} \partial_{\tilde{x}} (\tilde{u} \tilde{F}_r) = -\frac{1}{\epsilon^2} \tilde{F}_r, \quad (56)$$

where

$$\tilde{u} = \frac{u - u_g}{c}.$$

As for the system (44)-(45) we transform the previous system in a non-stiff hyperbolic system with stiff source term

$$\partial_{\tilde{t}} E_r + \partial_{\tilde{x}} (\tilde{u} E_r + \tilde{F}_r) = -\frac{1}{\epsilon^2} ((a T_m^4 - E_r) - \epsilon(1 - \epsilon) \partial_{\tilde{x}} (\tilde{u} E_r)), \quad (57)$$

$$\partial_{\tilde{t}} \tilde{F}_r + \partial_{\tilde{x}} (\chi E_r + \tilde{u} \tilde{F}_r) = -\frac{1}{\epsilon^2} \left( \tilde{F}_r + (1 - \epsilon^2) \partial_{\tilde{x}} \chi E_r + \epsilon(1 - \epsilon) \partial_{\tilde{x}} (\tilde{u} \tilde{F}_r) \right), \quad (58)$$

whose eigenvalues are

$$\tilde{\lambda}^{\pm} = \frac{\left( \epsilon \chi' \pm \sqrt{(\epsilon \chi')^2 + 4(\chi - f \chi')} \right)}{2} + \tilde{u}.$$

The same analysis as above leads to the following scheme

$$\frac{1}{\Delta t}(E_r^{n+1} - E_r^n)_i + \frac{1}{\Delta r}(F_{r,i+\frac{1}{2}}^* - F_{r,i-\frac{1}{2}}^*)^{n+\frac{1}{2}} = \sigma c(a_r T^4 - E_r)_i^{n+\frac{1}{2}} \quad (59)$$

$$\frac{1}{\Delta t}(F_r^{n+1} - F_r^n)_i + \frac{c^2}{\Delta r}(P_{r,i+\frac{1}{2}}^* - P_{r,i-\frac{1}{2}}^*)^{n+\frac{1}{2}} = -\sigma c F_{r,i}^{n+\frac{1}{2}} \quad (60)$$

where

$$\begin{aligned} F_{r,i+\frac{1}{2}}^* &= F_{r,i+\frac{1}{2}} + \epsilon \frac{\tilde{a}^+(u_{i+\frac{1}{2}} - u_g)E_i - \tilde{a}^-(u_{i+\frac{1}{2}} - u_g)E_{i+1}}{\tilde{a}^+ - \tilde{a}^-} \\ &+ \frac{(1-\epsilon)}{2} (u_{i+\frac{1}{2}} - u_g)(E_{r,i+1} + E_{r,i}), \end{aligned} \quad (61)$$

$$\begin{aligned} P_{r,i+\frac{1}{2}}^* &= \epsilon^2 P_{r,i+\frac{1}{2}} + \frac{(1-\epsilon^2)}{2} (P_{r,i+1} + P_{r,i}) \\ &+ \frac{\epsilon}{c^2} \frac{\tilde{a}^+((u_{i+\frac{1}{2}} - u_g))F_{r,i} - \tilde{a}^-((u_{i+\frac{1}{2}} - u_g))F_{r,i+1}}{\tilde{a}^+ - \tilde{a}^-} \\ &+ \frac{(1-\epsilon)}{2c^2} (u_{i+\frac{1}{2}} - u_g)(F_{r,i+1} + F_{r,i}), \end{aligned} \quad (62)$$

and

$$\tilde{a}^+ = \max(\tilde{\lambda}_{i+1}^+, \tilde{\lambda}_{i+\frac{1}{2}}^+, 0), \quad \tilde{a}^- = \min(\tilde{\lambda}_i^-, \tilde{\lambda}_{i+\frac{1}{2}}^-, 0). \quad (63)$$

In the previous discretization of the radiation subsystem, one need the value of  $\epsilon$  at each interface. In practical computations, where the opacity gradient can be large, we compute a value of  $\epsilon$  in each cell  $\epsilon = 1/\sigma\Delta x$ . The value of  $\epsilon$  at the interface is then taken to be the maximum value in the two adjacent cells. As we will see this method has given very satisfactory results even in the case of radiative shock with very strong opacity gradient.

Let us also remark that if we take  $\tilde{a}^\pm = \tilde{\lambda}_{i+\frac{1}{2}}^\pm$ , then the HLLE solver coincides with the Roe solver for the radiation subsystem. Thus, if we use for the hydrodynamic subsystem a Roe solver, then the above scheme is exactly the Roe scheme for the radiation-hydrodynamics system where the non conservative coupling terms are dropped. Nevertheless using HLLE solver for the radiation insures positivity of the scheme.

#### 4. ACTUAL IMPLEMENTATION OF THE METHOD

We present in this section how the full radiation-hydrodynamics system is discretized and integrated. As we mentionned before, when using system (1-5) the treatment of hydrodynamics is independant of the radiation (apart form the source terms) and has been described in section (3.2). For the radiative transfer in spherical coordinates the equations to be solved are the following:

$$\left\{ \begin{array}{l} \partial_t(E_r S) + \partial_r((u - u_g)E_r S) + P_r S \nabla \cdot u \\ = \kappa \rho c S (a_r T^4 - E_r) + \frac{u}{r} S (3P_r - E_r) \\ \partial_t(F_r S) + c^2 \partial_r(P_r S) + \partial_r((u - u_g)F_r S) + F_r S \partial_r u \\ = -\kappa \rho c F_r S + c^2 P_r \partial_r S - \frac{(3P_r - E_r)}{r} c^2 S \end{array} \right. \quad (64)$$

The left-hand sides of the previous system contains the  $M_1$ -radiation subsystem and coupling terms due to the comoving frame. We treat the conservative terms using the Godunov-type method presented in the previous section. The non-conservative coupling terms, which, as we have seen previously, do not modify the eigenvalues of the physical system, are discretized in the following way: the velocity divergence is discretized using the value of the velocity at the interface given by the hydrodynamic solver. The two terms of the right-hand-side are local and are computed by integration over the volume of the cell. All the terms of the second equation are discretized in the same manner. And finally, all terms (given by the hydrodynamic or radiation solver, comoving and source terms) are computed at the same time so that all equations are fully coupled in an implicit scheme. This is summarized in the following tables.

$\kappa\rho c S(a_r T^4 - E_r)$	$P_r S \nabla \cdot u$	$\frac{u}{r} S (3P_r - E_r)$
$(\kappa\rho c(a_r T^4 - E_r) \Delta v)_i^{n+\frac{1}{2}}$	$(P_r)_i^{n+\frac{1}{2}} (uS)_{[i \pm \frac{1}{2}]}^{n+\frac{1}{2}}$	$(\frac{u}{r} (3P_r - E_r) \Delta v)_i^{n+\frac{1}{2}}$

$\kappa\rho c F_r S$	$c^2 P_r \partial_r S$	$\frac{(3P_r - E_r)}{r} c^2 S$	$F_r S \partial_r u$
$(\kappa\rho c F_r \Delta v)_i^{n+\frac{1}{2}}$	$(c^2 P_r S)_i^{n+\frac{1}{2}}$	$\left(\frac{(3P_r - E_r)}{r} c^2 \Delta v\right)_i^{n+\frac{1}{2}}$	$(F_r)_i^{n+\frac{1}{2}} (uS)_{[i \pm \frac{1}{2}]}^{n+\frac{1}{2}}$

In order to gain in accuracy, we actually use a classical second order MUSCL method ([15]) to compute the flux. For the hydrodynamics *minmod* slopes are computed for  $\rho, u$  and  $P$ . For the radiative transfer, slopes are computed for  $E_r$  and  $f$  in order to always satisfy the constraint  $|f| \leq 1$ . These slopes are then used to extrapolate the value of the different fields near the cell interface. These extrapolated values are then used as inputs for the Riemann solvers and for the upwind flux.

Finally, as we will show in section 5.4, the CFL condition given by an explicit treatment of hydrodynamics is too much small in some applications and a full implicit treatment is needed. Then the non-linear system of equations (18), (27)-(29) and (64) is solved iteratively using a Raphson-Newton method. The jacobian matrix is computed using numerical derivatives. We use for the implicitation parameter  $\alpha = 0.55$ .

## 5. TEST CASES

We present in this section some test cases for the radiation-hydrodynamic scheme presented above. We start with some simple shock-tube problems and end with the collapse of a gas cloud leading to a stellar-like structure. All the shock-tube problems are performed using a constant and uniform resolution (i.e. eulerian grid) in order to place emphasis on the properties of the radiation-hydrodynamics solver.

### 5.1. Radiative front

We first look at the propagation of a radiative front in vacuum. In the initial conditions the half-space  $x < 0$  is filled with radiation with  $T_r = 10^4$  and  $f = 1$ . For the half-space  $x > 0$  we have  $T_r = 10^3$  and  $f = 1/3$ . The front should propagate at the speed of light and remain sharp. The results are presented on figure (3). We

first see that, thanks to the  $M_1$  model, the front propagates at the proper speed. After a propagation of 1cm (ie 100 cells) we see that the front has suffered from significant diffusion and is spread among about 20 cells. But, when it propagates further the spatial extension of the front remains roughly stable. This stability of the front is due to the fact that for  $f = 1$  the wave speed is equal to  $c$  while for  $f = 1/3$  it is equal to  $c/3$ . Therefore, contrary to a contact discontinuity, there is a slight compression of this radiative front.

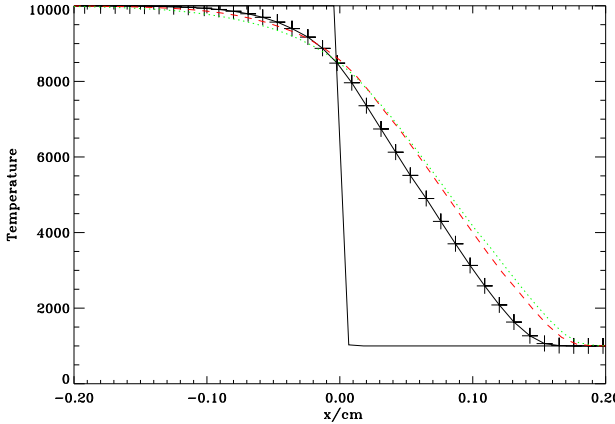


**FIG. 3** The radiative temperature in the initial conditions (solid line), after a propagation of 1cm (ie 100 cells) (black cross), 2cm (dashed line) and 3cm (dotted line). Each curve is shifted along the  $x$ -axis of  $-c\Delta t$ . Which means that since the front propagate at the speed of light the discontinuity should stay at  $x = 0$ .

We now test our scheme with radiative shocks playing particular attention to the stability of the solution for different sampling of the photon mean free path.

## 5.2. Radiative shock dominated by hydrodynamical pressure

We examine in this section a stationary strong shock in a gas with unit molecular weight and a constant opacity of  $\kappa = 4.0 \cdot 10^4 \text{ cm}^2/\text{g}$ . The upstream quantities for the gas are given by:

$$\rho = 1.2 \cdot 10^{-3} \text{ g/cm}^3 \quad T = 10 \text{ }^{\circ}\text{K} \quad u = 200 \text{ km/s} \quad T_r = T \quad F_r = 0. \quad (65)$$

As the upstream material is extremely opaque, any radiation incoming from the radiative front will be completely reabsorbed at some distance. Far from this area, the flow becomes homogeneous, the radiative flux vanishes ( $F_r = 0$ ), the radiation and the fluid temperatures are in equilibrium ( $T_r = T$ ).

The downstream quantities are chosen so that the Rankine-Hugoniot jump conditions are satisfied for the mass (1), total momentum (9) and total energy (10). Let us notice that in that case the Rankine-Hugoniot jump conditions for the complete coupled fluid radiative system (1 - 5) are not satisfied. As we introduce only three constraints on the downstream state, we need two extra relations to know this state (see Mihalas [11]). The downstream material is also extremely opaque, hence, we still have  $F_r = 0$  and  $T_r = T$ . In fact, the gas given by the downstream

or upstream states act as a real non perfect gas where the material pressure  $P$  is replaced by the total pressure  $P + P_r$  and where the material energy  $E$  is replaced by the total energy  $E + E_r$ . In this test, the equation of state is totally dominated by the gaz ( $\gamma = 5/3$ ) and radiation is only significant for energy transport.

The photon mean free path in the upstream material is given by  $\lambda = 1/\kappa\rho \simeq 0.02\text{cm}$ . The results of the simulation for a grid with  $\Delta x = 0.5\lambda$  are given in figure (4). The hydrodynamical shock is stable and is sampled over 2 cells and there is a large region in front of the shock where the gas is preheated by radiation. In this thermal precursor the gas is heated and slowed down by the energy released in the shock. We have looked at the behavior of this precursor under changes in resolution. We can see (figure (5-A)) that even when the mean free path of photon is not sampled, the thermal precursor keeps the proper spatial extension. If the numerical scheme is not modified to take into account the diffusion limit, the extension of the precursor is much too large, as was expected from the analysis made in (3.3.2). If the spatial sampling of the simulation is large compared to the length of the precursor, the temperature jump is captured over 2 or 3 cells which is roughly as accurate as the treatment of a shock.

### 5.3. Shock dominated by radiative pressure

We now examine the case of a shock where the dynamical influence of radiation is not limited to energy transport. In this test case, the energy in the downstream region is dominated by the radiative energy. The upstream conditions are:

$$\rho = 10^{-3} \text{ g/cm}^3 \quad T = 10^5 \text{ }^{\circ}\text{K} \quad u = 1000 \text{ km/s} \quad T_r = T \quad F_r = 0.$$

and the downstream conditions are given by the Rankine-Hugoniot relations as detailed in the above section. As in the previous test we assume for the radiation that downstream states are at equilibrium, (i.e.  $E_r = a_r T^4$  and  $F_r = 0$ ).

The gas molecular weight is, as before, set to unity and the opacity is  $\kappa = 1 \text{ cm}^2/\text{g}$ . The photon mean free path in the upstream region is therefore  $\lambda = 1/\kappa\rho = 10^3 \text{ cm}$ . The results of this test case for  $\Delta x = 0.5\lambda$  are presented on figure (6). As in the previous case, the shock is captured in two cells and there is a large preheated region in front of the shock. In this region, energy is transferred from the gas to the radiation and the radiation energy density quickly dominates as the temperature rises. In the upstream region the equation of states is dominated by the gaz ( $\gamma = 5/3$ ) and in the downstream region it is dominated by radiation ( $\gamma = 4/3$ ). In this case the effective  $\gamma$  in the downstream region is  $4.2/3$ . Eventhough we do not explicitly treat the total (gaz and radiation) conservation law this energy transfer is treated correctly. As in the previous case, the shock is absolutely stable and the Rankine-Hugoniot relations are strictly verified. This example illustrates the fact that eventhough our hyperbolic analysis decouples matter and radiation, our scheme is valid even when there are large momentum and energy transfer between gas and radiation. In figure (7) we have plotted the temperature profile for different grid resolutions to illustrate the proper behavior of our scheme in both the streaming and diffusion regime.

### 5.4. Collapse of a gas cloud

Star formation is a very challenging problem, where radiation transport plays a dominant role. The modeling of the formation of a star introduces a wide range of

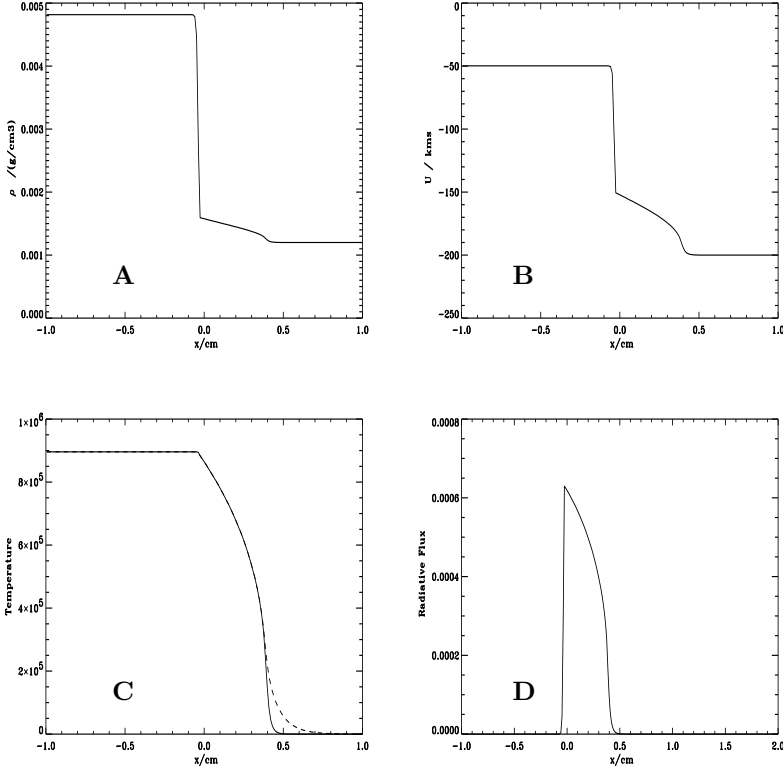


**FIG. 4** Profiles of density (A), velocity (B), gas (solid line) and radiation (dashed line) temperatures (C) and radiative flux (D) for a strong shock with negligible radiative energy density.

length and time scales. The mean density contrast between a collapsing cloud and the star reaching main sequence is about  $10^{20}$ . The initial cloud radius is about  $10^{18}\text{cm}$ , while the typical radius of a solar-like star is less than  $10^{11}\text{cm}$ . The compactness of the star embryo requires a spatial resolution of at least  $\Delta r/r \simeq 10^{-4}$  in the envelope outer layers, where the pressure gradients are the highests. This means that the Courant number corresponding to a dynamical time scale  $t_d = r/c_s$ , where  $c_s$  is the sound speed, is about  $C = 10^4$ . If the evolution of the system is to be followed over the Kelvin-Helmotz time scale,  $t_{K-H} = GM^2/RL \simeq 30\text{Myr}$  for a solar-like star, the Courant numbers we have to deal with is of the order of  $10^{14}$ . These rough estimates demonstrate that the spatial resolution required for our problem demands an implicit numerical scheme. The process of star formation is dominated by the properties of radiative transfer in highly unsteady flows. The reason is that self-gravity alone can not lead to the formation of a compact object unless the energy released by gravitational contraction beeing radiated away, from the surface of the protostellar core. Energy transport in the core's interior, towards

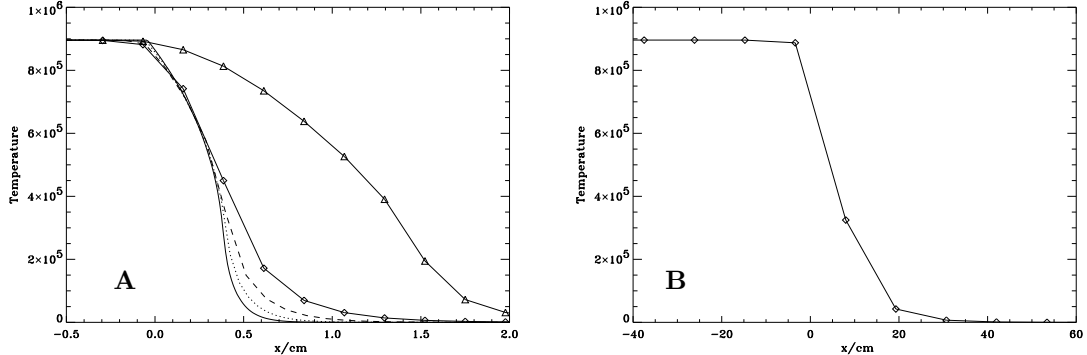


**FIG. 5** Profiles of gas temperature in the upstream flow preheated by the radiation. In plot A the grid spacing was  $\Delta x = 0.5\lambda$  (solid line),  $2.5\lambda$  (dotted line),  $5.5\lambda$  (dashed line),  $11\lambda$  (solid line with squares). The solid line with triangle is the results of a simulation with  $\Delta x = 11\lambda$  but where  $\epsilon$  was kept to unity. For the simulation of plot B the grid spacing was  $550\lambda$ , the thermal precursor is now sampled on 2-3 grid points which is almost as accurate as the treatment of a shock.

the photosphere, is mainly due to radiative transfer in an optically thick plasma, and convection. The photosphere is a narrow layer where the radiation transport regime abruptly turns from the diffusion regime to the free streaming regime, by which energy flowing from the core by diffusion and convection is radiated away. Furthermore, during the accretion phase, the photosphere is surrounded by super-critical radiating accretion shock, where the kinetic energy of the infalling gas is essentially converted into outgoing radiation. Since most of the total luminosity of the protostar is produced within this sharp, optically thin accretion shock, the calculation of the structure of the radiative accretion shock is a crucial issue in the modeling of star formation. A correct evaluation of the entropy extracted by escaping radiation from the accreting material, deposited on the protostar surface, is also the key factor which determines the structure of the growing stellar core. First, the entropy profile determines the size of the quasistatic core, and hence determines the location of the protostar in the Hertzsprung-Russell diagram by the end of the accretion phase; second the entropy gradient triggers the highly efficient convective energy transport, in regions where  $\nabla s < 0$ , where  $s$  is the specific entropy.

We present in the following section an example of the calculation of the formation of a primordial star, in a slightly bound region of an overall expanding universe. The simple model presented here includes only hydrodynamics, gravitation and, of course, radiative transfer. It is nevertheless a very challenging test for radiative transfer. As we will see, the opacity gradients are very large and there is a steep transition from the diffusion to the free-streaming regime.

We start with a  $10^6$  solar mass gas cloud. The velocities are those of the homogeneous expansion of the universe (i.e.  $u(r) = H r$ , where  $H$  is the Hubble constant). The average density is the critical density and the density profile is smooth with a small central overdensity. We start our simulation at a redshift of 100 and the amplitude of the initial perturbation is adjusted so that the central

object forms at a redshift of 30. Initially the radiative energy density is that of the cosmic microwave background and the temperature of the gas is equal to the temperature of the radiation.

In a first phase the entire cloud is in expansion. Then, at a redshift of 50 the central part of the cloud starts to collapse. The central density increases, but the temperature remains almost constant because the energy is evacuated by radiation since the photon mean free path is much larger than the typical scale of the forming structure. Next, at a redshift of about 30, the central region is dense enough to become opaque to radiation. The temperature and the pressure start to grow and become large enough to prevent the collapse in the central region. Finally the infalling matter creates an accretion shock on the central core. The structure of the flow when the central density has reached  $x.10^{-8} g/cm^3$  is presented in figures (8) to (14).

The density profile is plotted in figure (8). The center is almost at the hydrostatic equilibrium and is surrounded by a slowly contracting envelope. The envelope ends at the accretion shock where the density jump is very important (about one order of magnitude) due to the fact that the gas radiates most of its energy, as is illustrated by figures (10) and (14). One can notice that the density contrast between the center and the outer accretion flow is of more than 18 decades and that the length scale vary of about 10 decades.

The velocity profile (figures (9)) shows that the outer region of the cloud is still expanding, following the global expansion of the universe. On the contrary, the inner region is gravitationally bounded and is collapsing. The accretion shock is clearly visible and is sampled over only one computational grid point. Due to the moving grid, the central part and the region of the shock have a high spatial resolution. The actual resolution profile can be seen on figure (13). In the central part of the cloud, the radiation is in the diffusion limit and the luminosity slowly increase (figure (10)). At the shock there is a very sharp increase in luminosity due to the fact that the gas is heated at the shock and radiates most of its energy. The luminosity is then constant except for the outer region where the luminosity of the cosmic microwave background starts to dominate. As is illustrated by figure (11), the radiation is in the diffusion regime in the central part of the cloud where the photon mean free path is much smaller than the radius while it is clearly in the free-streaming regime in the outer part. The transition between these two regimes occurs in a very sharp way at the shock. Figure (14) shows a zoom of the gas and radiation temperatures profiles near the shock. The spike in the gas temperature is a characteristic feature of supercritical radiative shock and a very high spatial resolution is needed to resolve it. Finally, the profile of the Eddington factor is plotted on figure (12). The Eddington factor is equal to one third in the central object, which confirm the fact that the diffusion regime is valid in this region. Then, there is a small jump at the shock and the Eddington factor grows as one goes away from the surface of the star. At large distance, the light coming from the star is blurred into the cosmic microwave background and the Eddington factor decreases back to one third. These large variations of both the Eddington factor and the opacity illustrate the interest of the  $M_1$  model for such radiative shock.

## 6. CONCLUSION

We have presented in this paper a new numerical model for radiative transfer which gives satisfactory results in a wide range of physical conditions including both

the diffusion and the free-streaming regimes where the anisotropy of the photons distribution function can be large. This method is therefore well suited to modeled some laser experiments and many astrophysical flows. Works are in progress to incorporate in the model a more detailed description of the physical processes (multigroup approach, ionization, ....) and to further develop this approach in a multidimensionnal framework.

## REFERENCES

- [1] D. S. BALSARA, *An Analysis of the Hyperbolic Nature of the Equations of Radiation Hydrodynamics*, J. Quant. Spectrosc. Radiat. Transfer, 61(5):617-627, 1999.
- [2] W. DAI AND P. WOODWARD, *Numerical Simulations for Radiation Hydrodynamics. I. Diffusion Limit*, J. Comput. Phys. 142,182-207, (1998).
- [3] W. DAI AND P. WOODWARD, *Numerical Simulations for Radiation Hydrodynamics. II. Transport Limit*, J. Comput. Phys. 257,199-233, (2000).
- [4] E.A. DORFI AND L. O'C. DRURY, Journal of Computational Physics, **69**, 175-195, 1987
- [5] B. DUBROCA AND J.-L. FEUGEAS, CRAS, **329**, 915-920, 1999
- [6] B. EINFELDT, C.D. MUNZ, P.L. ROE AND B. SJÖGREEN *On godunov-type methods near low densities*, J. Comput. Phys.,**92**,273, 1991
- [7] E. GODLEWSKI AND P.-A. RAVIART, *Numerical approximation of hyperbolic systems of conservation laws*, Springer-Verlag, New-York, 1996
- [8] S. JIN, L. PARESCHI ET G. TOSCANI, *Uniformly accurate diffusive relaxation schemes for multiscale transport equations*, SIAM J. Num. Anal., **38**, 913, 2000
- [9] E. LARSEN, J. MOREL, AND W. MILLER *Asymptotic Solutions of Numerical Transport Problems in Optically Thick, Diffusive Regimes*, J. Comput. Phys. 83 (1):212-236, 1989.
- [10] R. B. LOWRIE, J. E. MOREL AND J. A. HITTINGER, *The Coupling of Radiation and Hydrodynamics*, The Astrophys. J. (521):432-450, 1999.
- [11] D. MIHALAS AND B. WEIBEL-MIHALAS, *Foundation of Radiation Hydrodynamics*, Oxford University Press, 1984.
- [12] G. C. POMRAMING, *The Equations of Radiation Hydrodynamics*, Pergamon Press, 1973.
- [13] P.L. ROE, *Approximate Riemann solvers, parameter vectors, and difference schemes*, J. Comput. Phys.,**43**,357, 1981
- [14] E.F. Toro, “Riemann solvers and numerical methods for fluid dynamics”, springer, 1999
- [15] B. VAN LEER, *Toward the Ultimate Conservative Difference Scheme. V. A Second Order Sequel to Godunov's method*, J. Comput. Phys. 32 101 (1979).

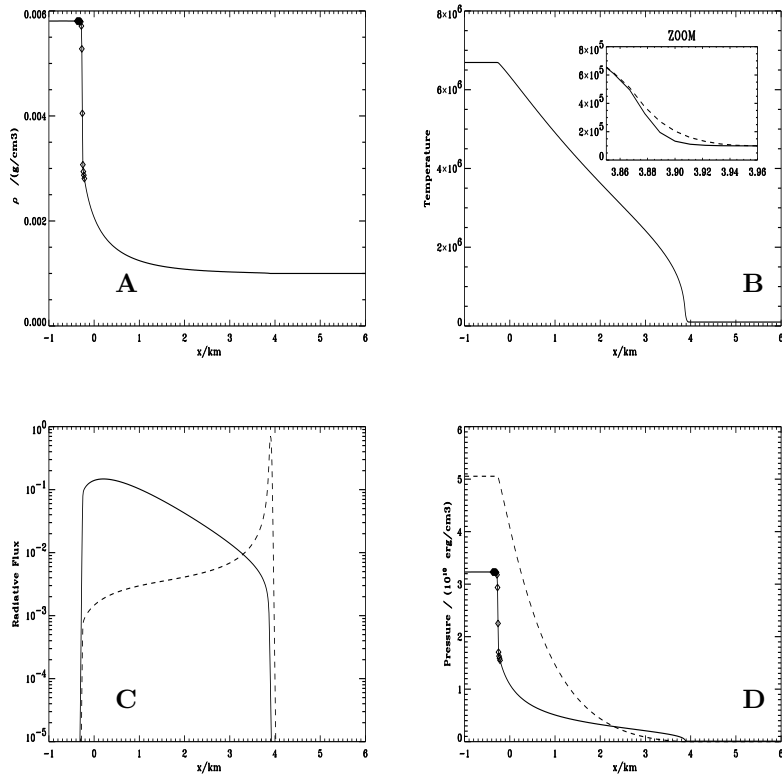


**FIG. 6** Profiles of density (A), gas (solid line) and radiation (dashed line) temperatures (B), radiative flux (in arbitrary units, solid line) and reduce flux (dashed line) (C) and gas (solid line) and radiative (dashed line) pressures (D) for a strong shock where the downstream energy is dominated by radiative pressure. The squares for the gas density and pressure show that even though the radiative pressure dominates the hydrodynamical shock is still properly treated.

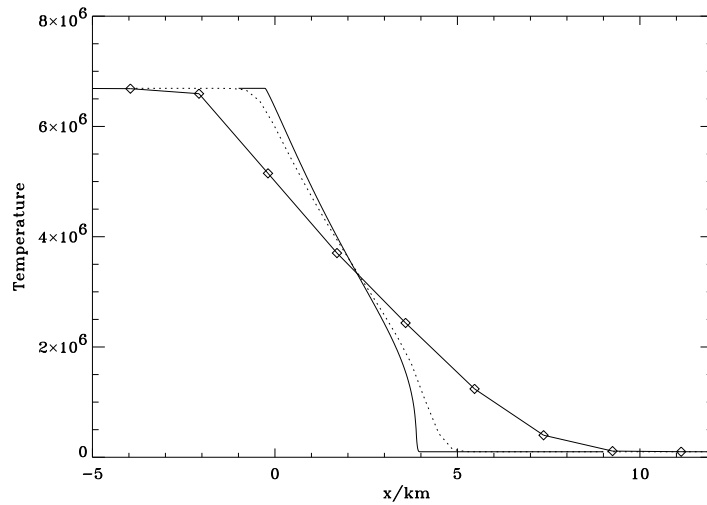


**FIG. 7** Profiles of temperature in the upstream flow preheated by the radiation. The grid spacing was  $\Delta x = 0.5\lambda$  (solid line),  $35\lambda$  (dotted line),  $200\lambda$  (squares).

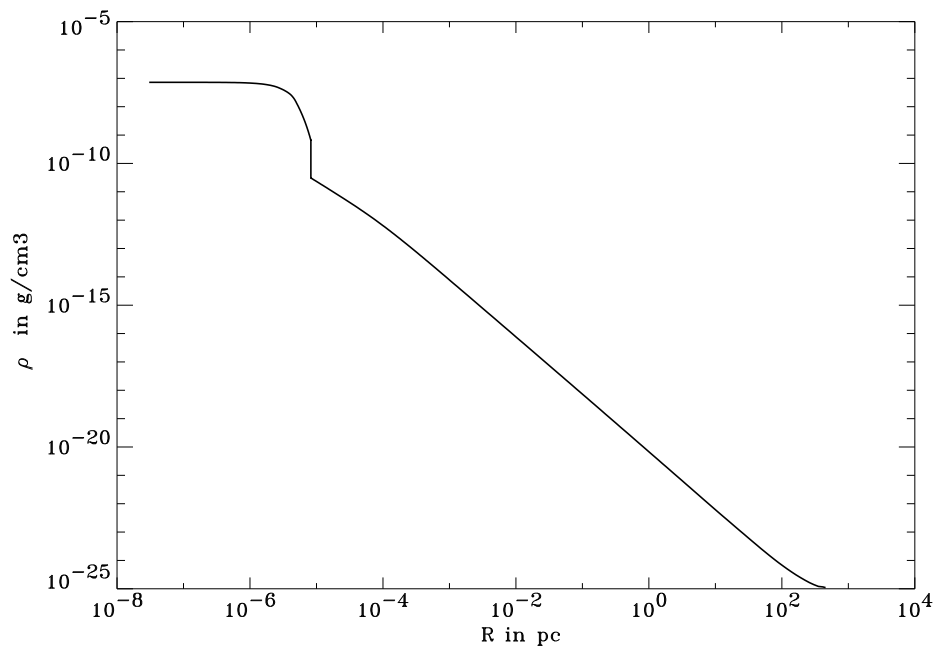


**FIG. 8** Density profile of the forming star.

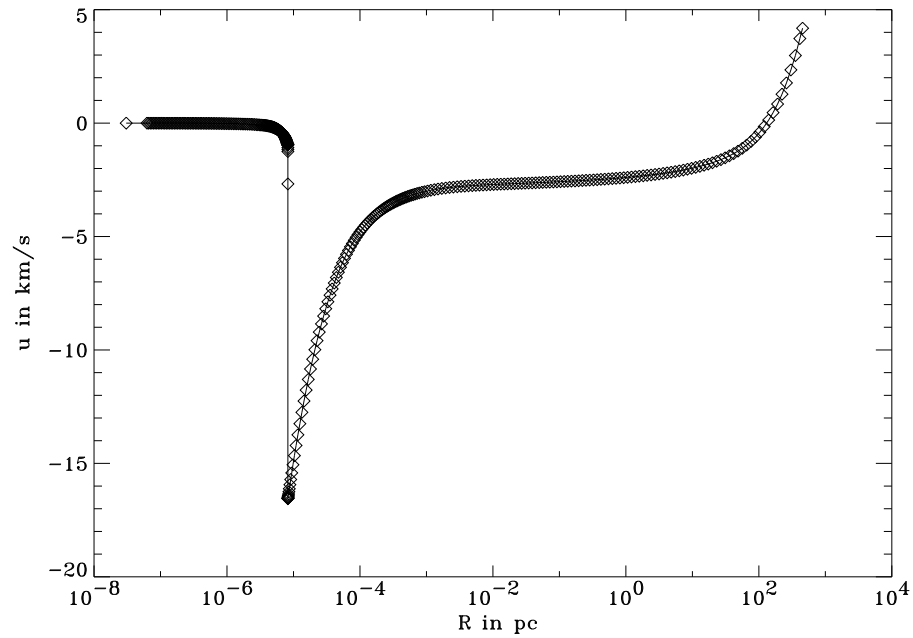


**FIG. 9** Velocity profile of the forming star.

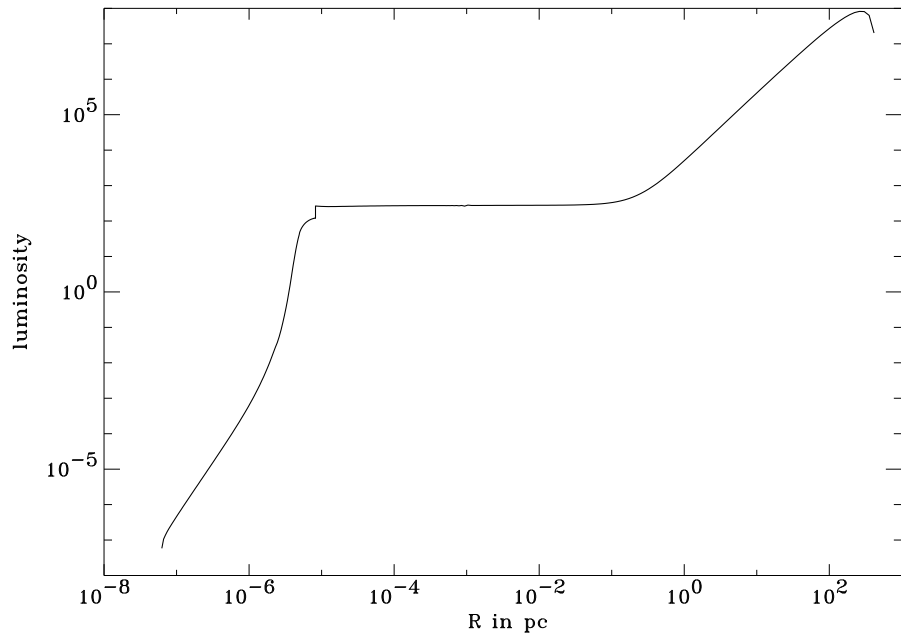


**FIG. 10** luminosity profile of the forming star.

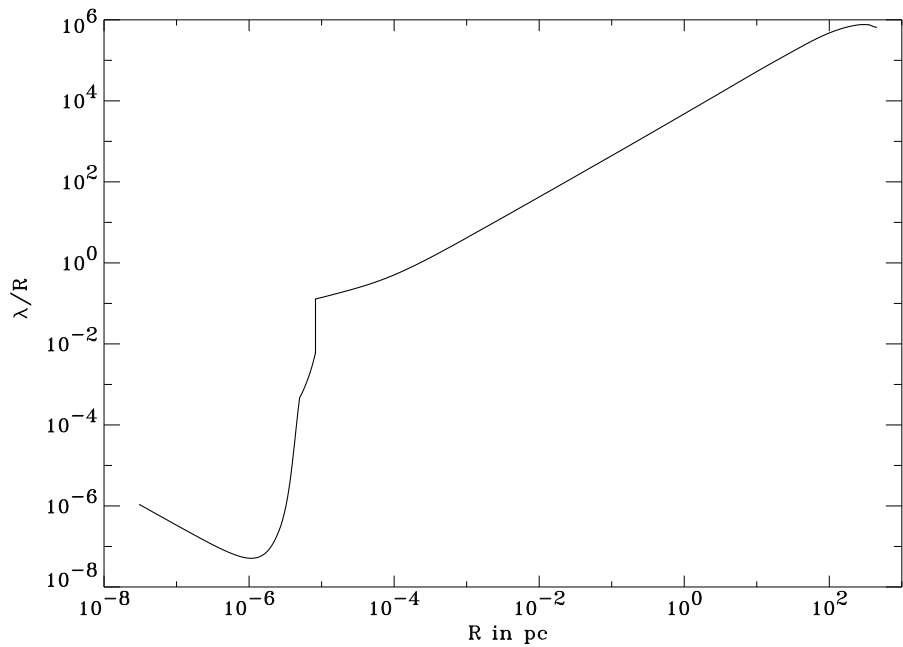


**FIG. 11** This plot represents the ratio of the photon mean free path over the radius as a function of the radius. This ratio is very small in the center where the coupling between matter and radiation is very strong, and it is very large in the outer region where the gas is transparent. This parameter varies over 10 orders of magnitude, with a sharp discontinuity at the shock, where the transition between the diffusion and the free streaming regime occurs.

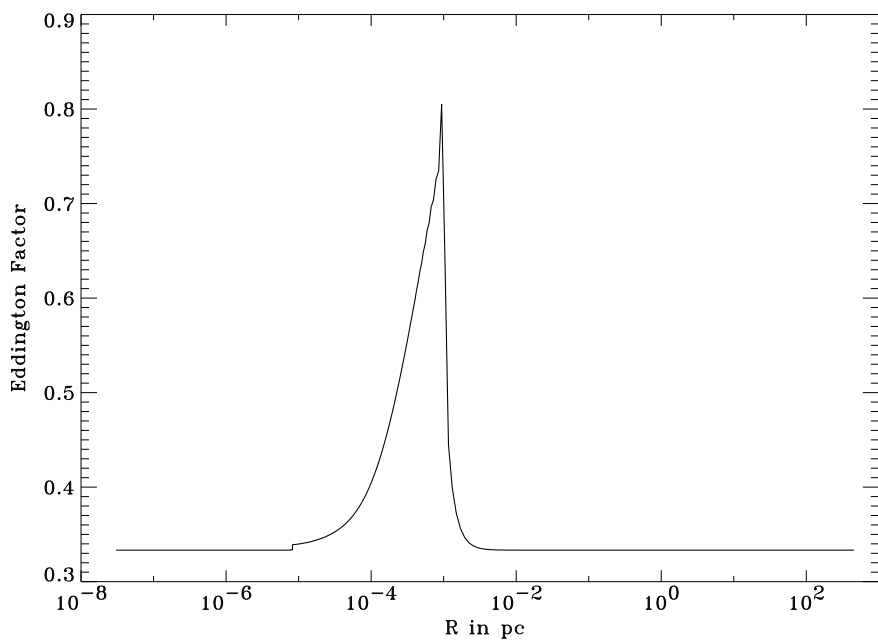


**FIG. 12** Profil of the Eddington factor.

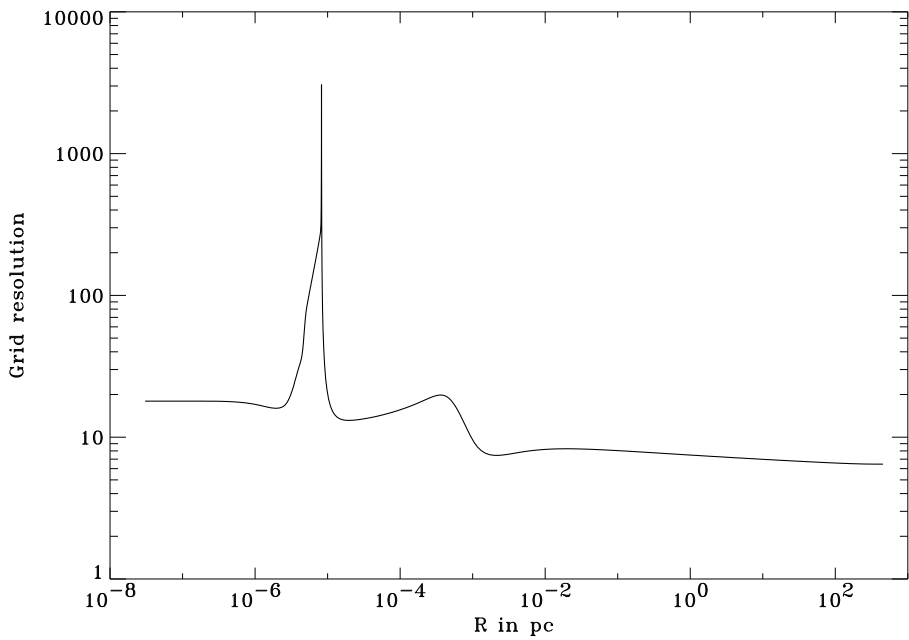


**FIG. 13** Profil of the grid resolution. The grid resolution is very high at the shock, where all the gradients are very large. With the high resolution it is possible to see the temperature spike at the shock (see figure (14)). The resolution is also important in the center to properly sample the pressure gradient and near the peak of the Eddington factor.

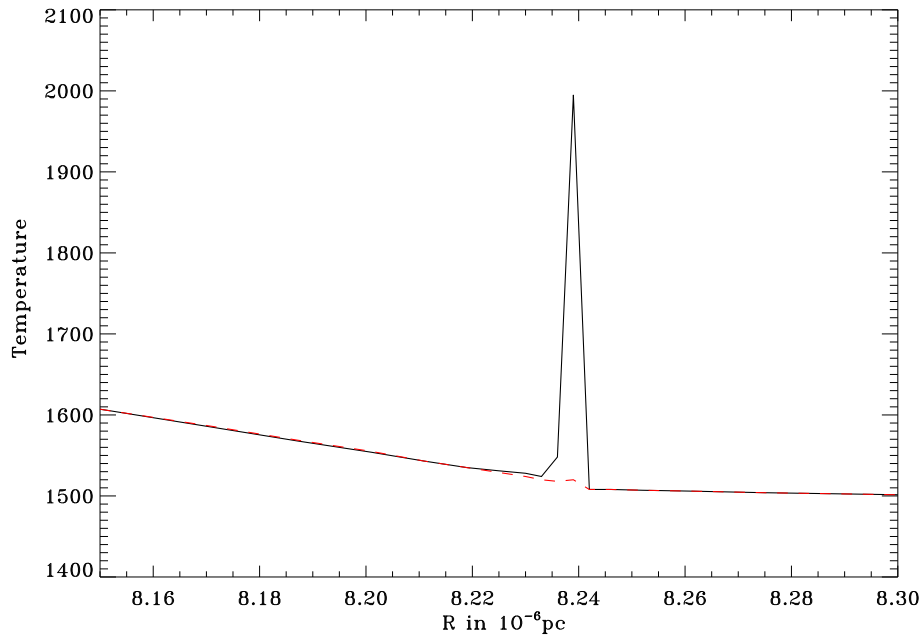


**FIG. 14** Temperature profiles at the shock. The gas is heated by the shock and then very quickly radiates its internal energy. This results in the large spike in the gas temperature at the shock which is associated to the jump in luminosity. On the contrary, the radiation temperature varies smoothly through the shock, it only changes its slope.